Electronic Supplementary Material (ESI) for Environmental Science: Nano.

Supporting Information

Real-time Monitoring of Magnetic Nanoparticle-assisted Nanoplastic Agglomeration and Separation from Water

Philipp Groppe, Susanne Wintzheimer, Andreas Eigen, Henrik Gaß, Markus Halik, and Karl Mandel*

Measurement principle of magnetic particle spectroscopy

In magnetic particle spectroscopy (MPS), an alternating sinusoidal magnetic field is used to induce a magnetization in the measured sample (Fig. S1a, b, here shown: magnetization curve with non-linear behavior). The magnetization behavior significantly depends on the magnetic properties (dia-, para-, ferro-, superparamagnetic, etc.) of the measured sample. The obtained magnetization is measured as a function of time (Fig. S1c). The alternating excitation field and the corresponding magnetization of the sample induce a voltage in the pick-up coils inside the measurement device (Fig. S1d). The obtained signal (overall induced voltage U_i) contains the excitation (U_e) and sample signal (U_p, Fig. S1e, f). By applying Fourier transform to the combined signal, the amplitude is obtained as a function of odd harmonics (Fig. S1g). The first harmonic is significantly influenced and governed by the excitation signal of the device and by dia- and paramagnetic materials (linear magnetization behavior, see Fig. S1h). However, higher harmonics are only influenced by the non-linear magnetization behavior, e.g. ferro-, ferri-, and superparamagnetic materials, which are used in this work (Fig. S1i). This allows the investigation of materials with non-linear magnetic properties by analyzing the signal constitution of higher harmonics. The obtained signal can then be displayed as a point curve with decaying harmonic amplitude.

The absolute intensity depends strongly on the characteristics of the samples. Additionally, it is also affected by factors like amplitude and frequency of the external magnetic field, the mass of the measured material, and pick-up coils' sensitivity. By normalization of measurement data on a suitable harmonic (Fig. S1j), these effects can be excluded and the material properties and interactions with surroundings become the dominating factors.

For more insights into MPS and its possibilities, we refer to literature.[1–6]

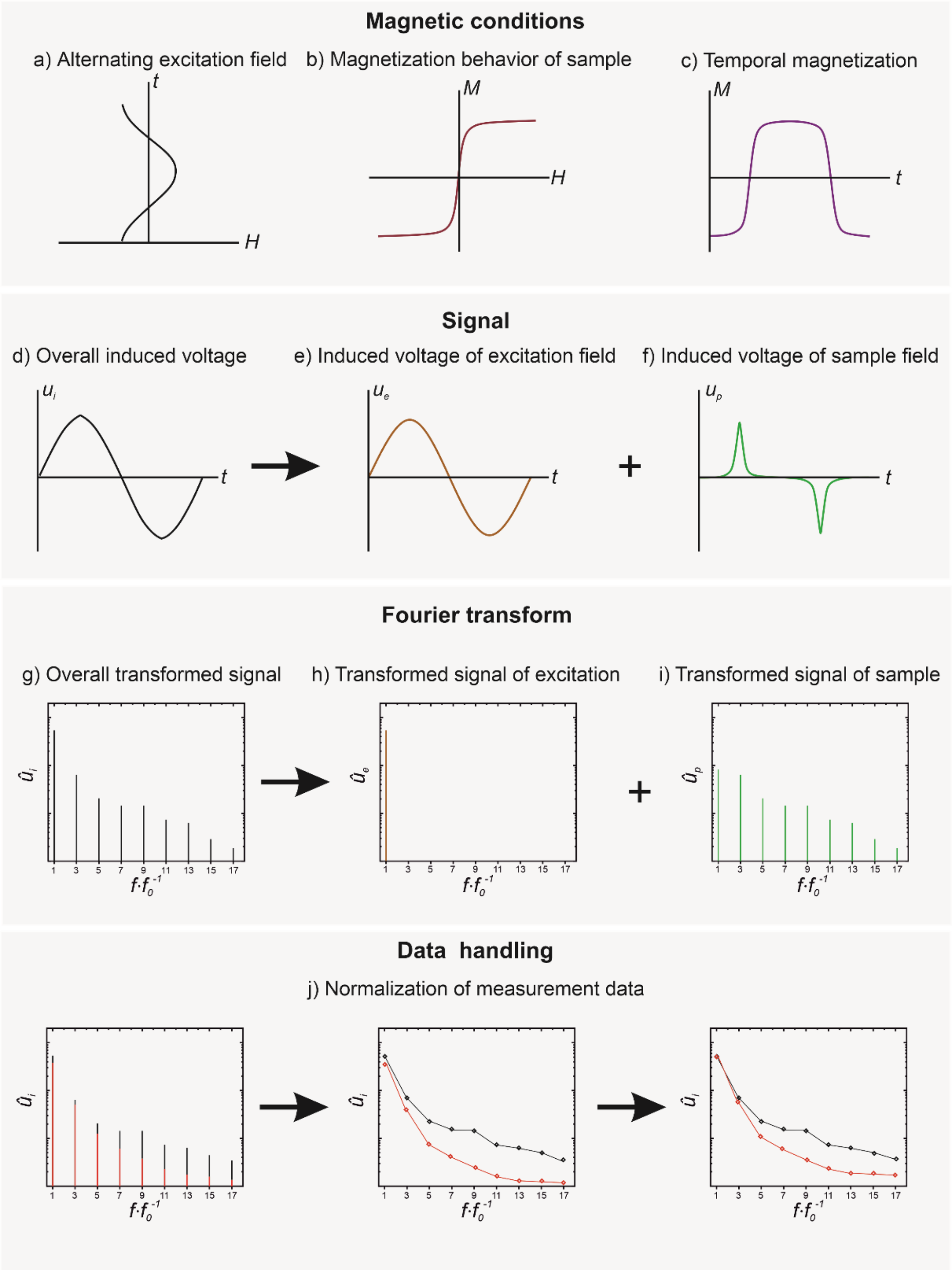

Fig. S1: Measurement principle of magnetic particle spectroscopy with the magnetic conditions of alternating excitation field (a), the non-linear magnetization behavior of the sample (b), and temporal magnetization (c) inside the measurement device. The overall induced signal (d) consists of a contribution of the excitation field (e) and the samples' magnetic field (f). Fourier transform generates a frequency-dependent measurement signal (g) with contributions from the excitation (h) and the sample (i). Normalization of the obtained signal curves (j) excludes influences from the setup and varying particle mass on the absolute signal intensity.

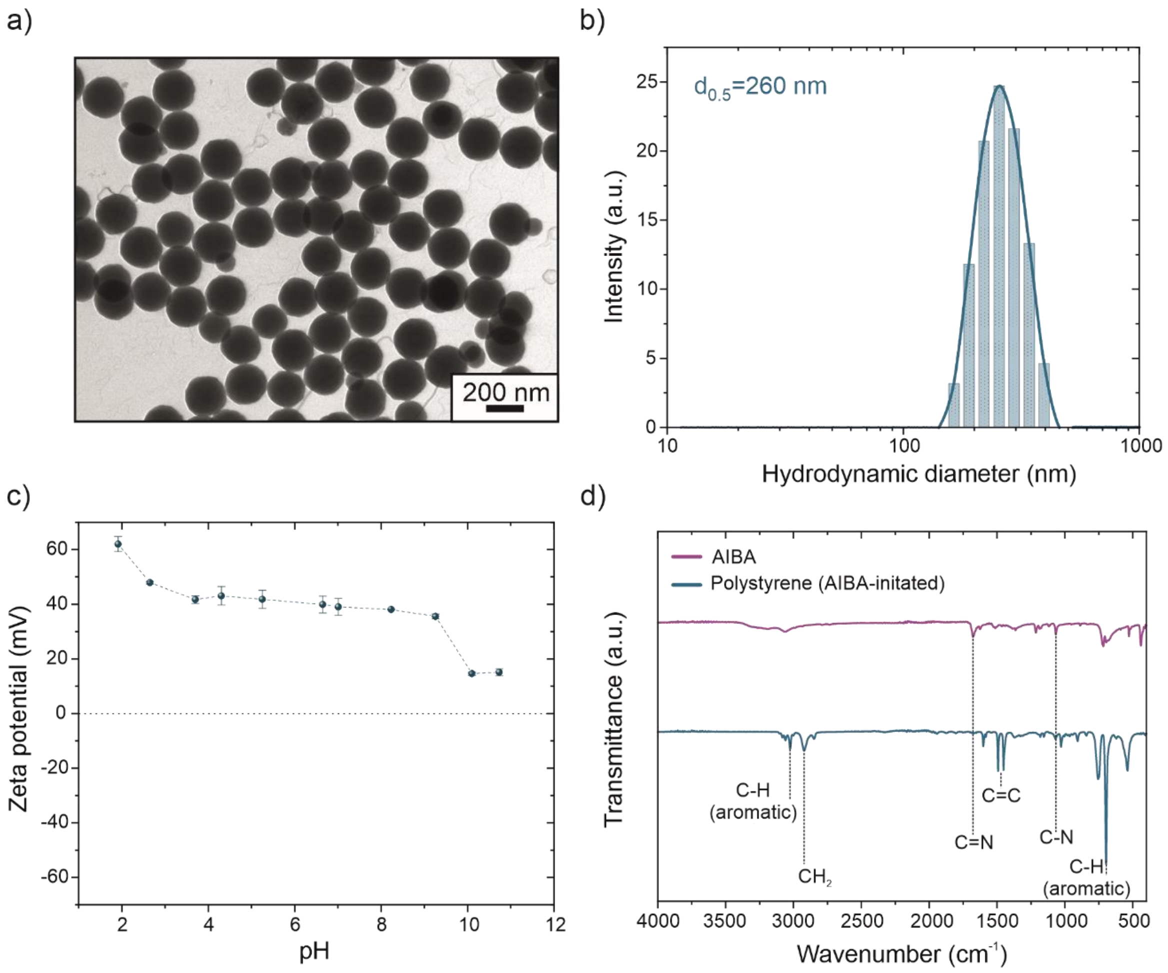

Fig. S2: Characterization of AIBA-initiated polystyrene nanoparticles, synthesized by emulsion polymerization. The nanoparticle size was determined by STEM analysis (a) to be 208±16 nm and the hydrodynamic diameter was found to be $d_{0.5}$=260 nm by DLS measurements (b). Zeta potential measurements (c) showed a positive surface potential over the investigated pH range. FTIR analysis (d) indicated the typical aromatic signals of polystyrene (aromatic system: aromatic C-H stretching ~3000-3100 cm^{-1}, C=C stretching ~1400-1600 cm^{-1} and C-H bending ~700 cm^{-1}; aliphatic system: CH_2 vibrations ~2850-2950 cm^{-1}). Only slight signals of the AIBA-based surface groups may be detectable (amine: C-N stretching ~1060 cm^{-1}; imine: C=N stretching ~1670 cm^{-1}).

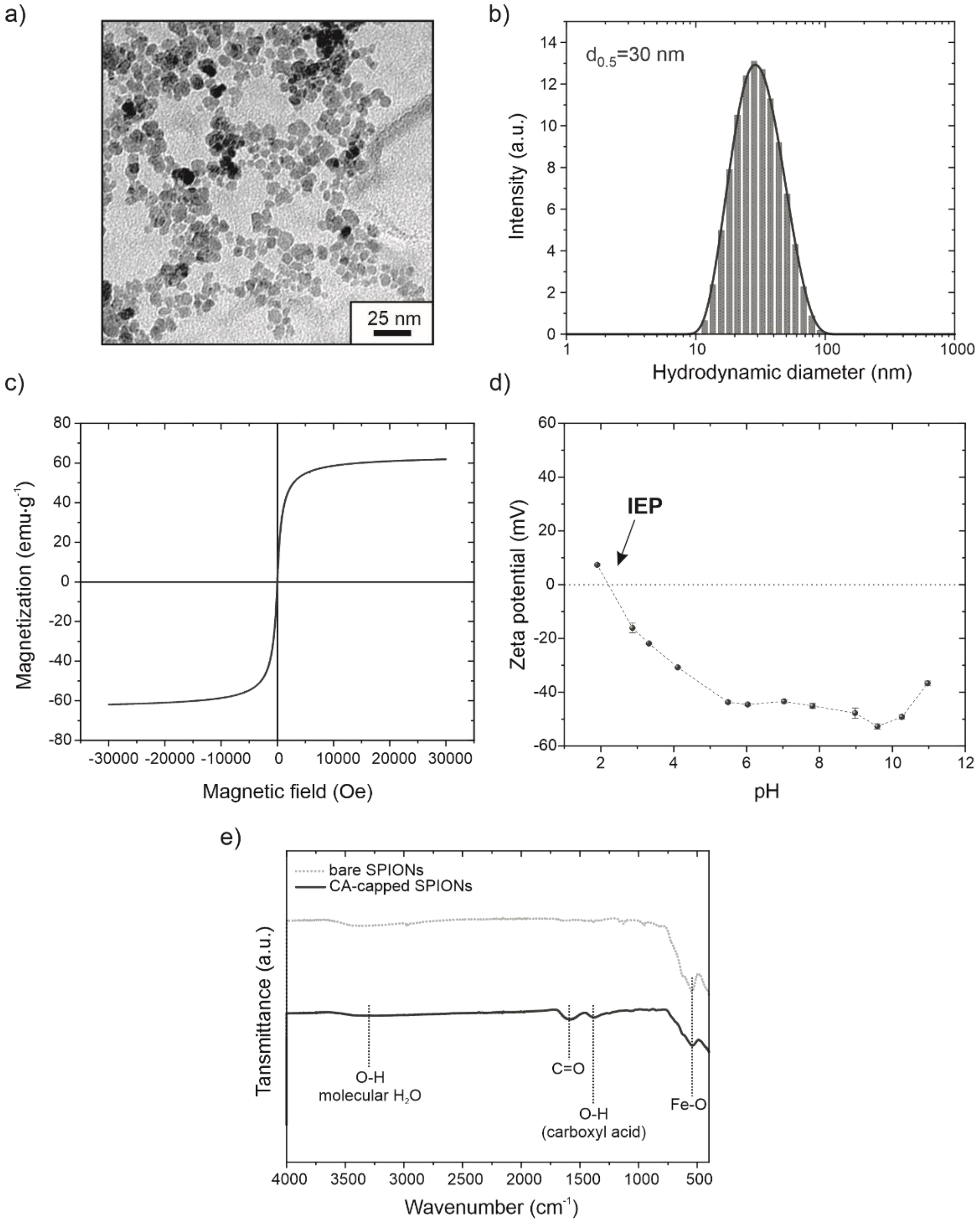

Fig. S3: Characterization of citric acid-capped SPIONs. The nanoparticle size was determined by TEM analysis (a) to be 9±2 nm and the hydrodynamic diameter was found to be $d_{0.5}$=30 nm by DLS measurements (b). SQUID measurements (c) revealed the superparamagnetic behavior of the synthesized nanoparticles with a saturation magnetization of 62 emu g^{-1}. Zeta potential measurements (d) showed a negative surface potential between pH~3 and pH~11. FTIR analysis (e) confirmed the capping of SPIONs with the citric acid (carboxyl acid: O-H bending ~1390 cm^{-1}, C=O stretching ~1580 cm^{-1}, O-H stretching ~2500-3300 cm^{-1}; molecular H_2O: O-H stretching ~3000-3500 cm^{-1}; iron oxide: Fe-O vibrations ~550 cm^{-1}).

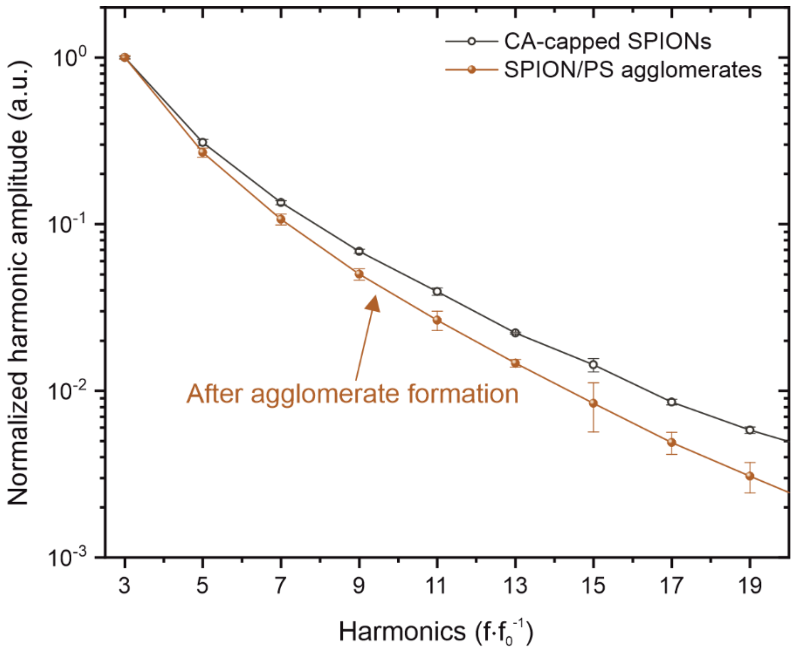

Fig. S4: Exemplary MPS curves of *in-situ* measurements before (greyish line and data points) and after (brownish line and data points) addition of oppositely charged PSNPL. The induced agglomeration is indicated by a faster signal decay.

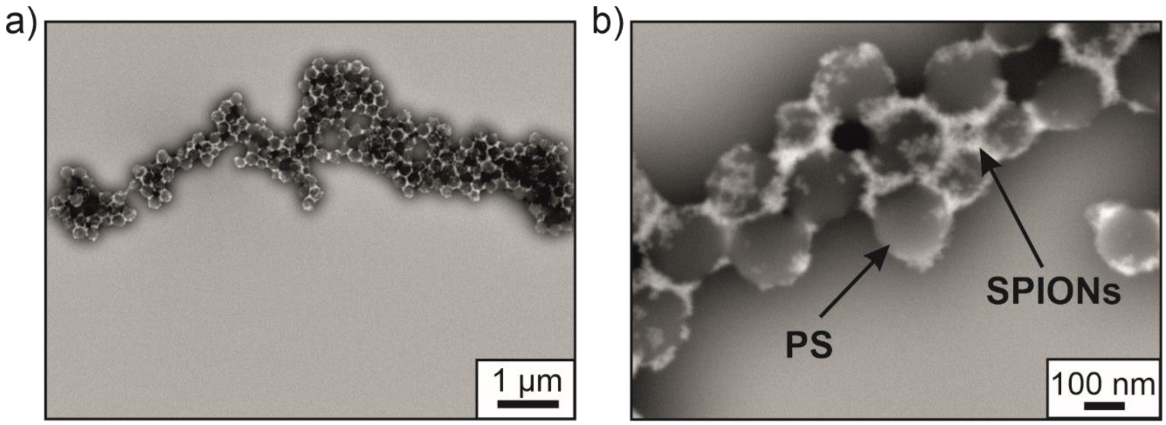

Fig. S5: Overview (a) and detail (b) BSE-SEM micrographs of formed agglomerates between positively charged PSNPL and negatively charged SPIONs during *in-situ* measurements.

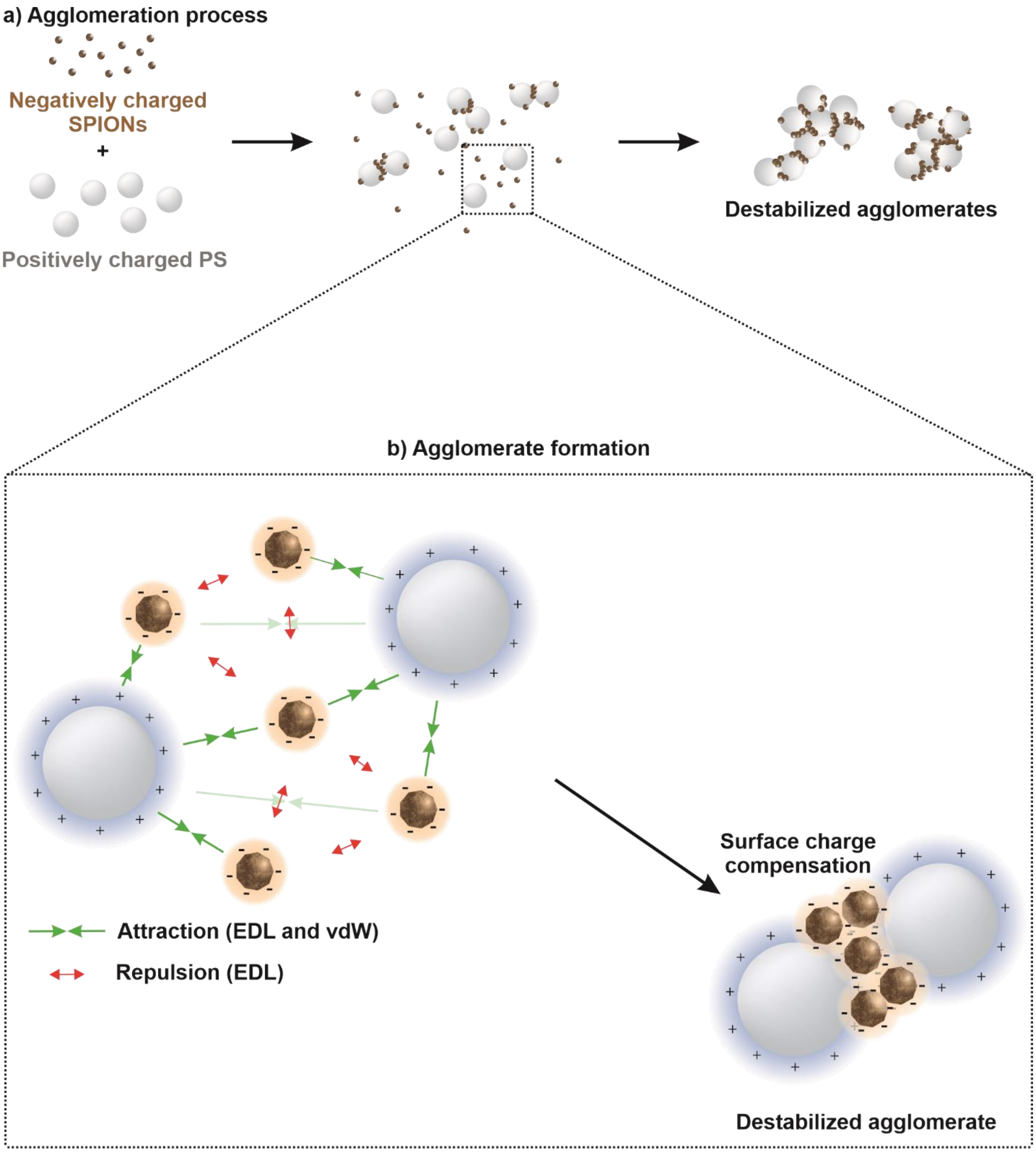

Fig. S6: Schematic illustration of the agglomeration process taking place between SPIONs and PSNPLs with oppositely charged surfaces when mixed in water (a). Detailed scheme of the agglomerate formation caused by electrostatic (EDL) and vdW attraction according to the DLVO theory. The interparticle attraction (between PSNPLs and SPIONs) and subsequent charge compensation could outweigh the repulsion between single magnetic agglomeration agent's eventually leading to neck-like assemblies like observed.

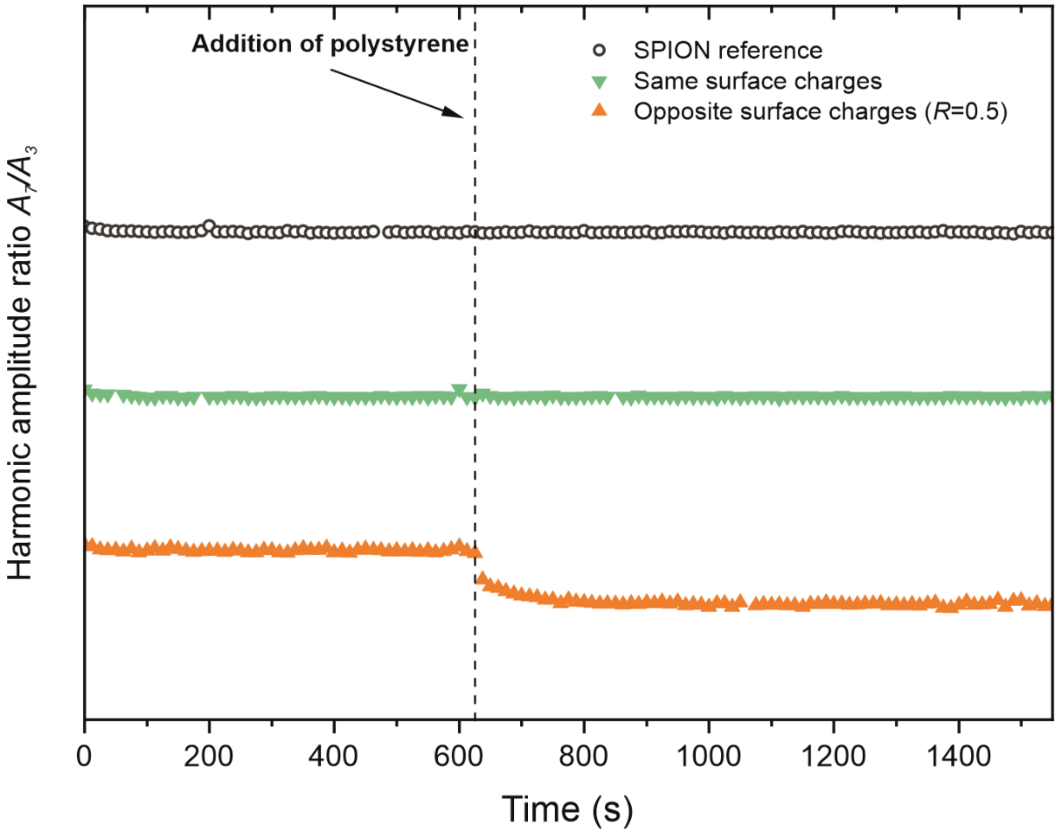

Fig. S7: Time-dependent MPS measurement curves of pure CA-capped SPIONs (grey), CA-capped SPIONs with addition of PSNPL with the same surface charge (green), and CA-capped SPIONs with addition of oppositely charged PSNPL (orange). When electrostatic repulsion is sustained, no agglomeration and, thus, no structural change occurs that would lead to a signal decay over time. In the case of oppositely charged nanoparticles, the decay becomes visible right after addition of the PSNPL particles.

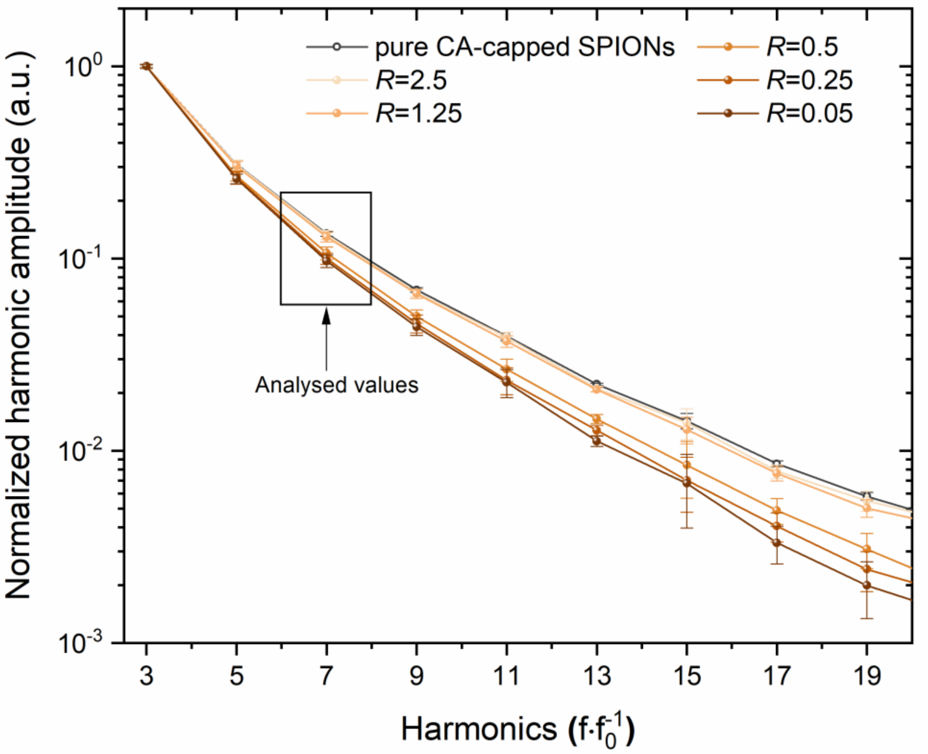

Fig. S8: MPS signal curves for all investigated *R*-values at pH~3.2. The 7th harmonic was chosen for the investigation of the signal change with increasing SPION content. With increasing SPION content the signal curves approach the one of the pure CA-capped SPION reference, indicating a difference in the structure of formed agglomerates and residual SPIONs not involved in agglomeration.

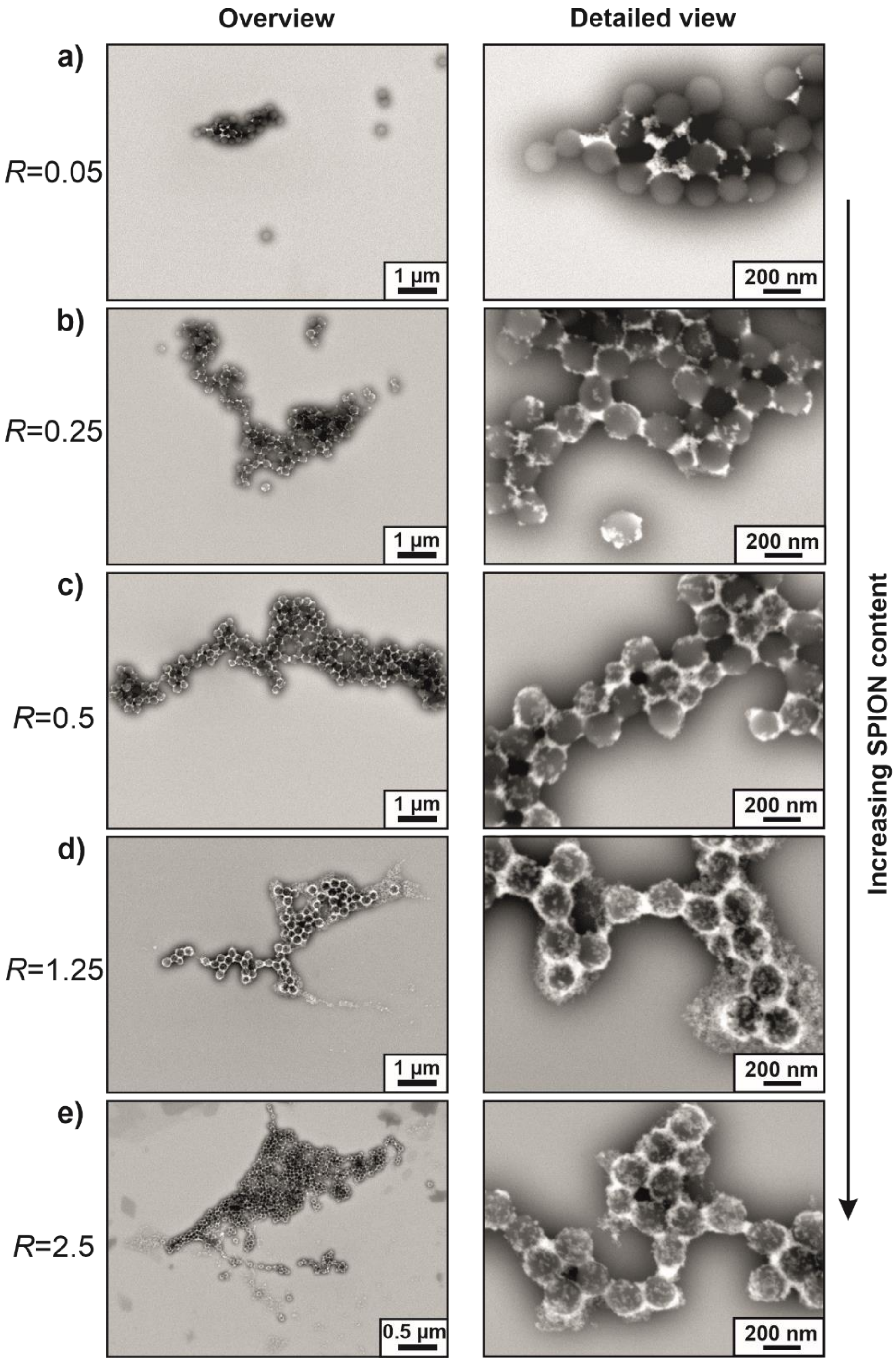

Fig. S9: Overview (left array) and detail (right array) BSE-SEM micrographs of formed agglomerates for *R*-values of 0.05 (a), 0.25 (b), 0.5 (c), 1.25 (d), and 2.5 (e) at pH~3.2. For all ratios, a similar structure with SPIONs clustering around the PSNPL is observed. Agglomerate network formation takes place independently of the SPION content. By increasing particle ratio, a continuous distribution of SPIONs across the PSNPL particles becomes visible.

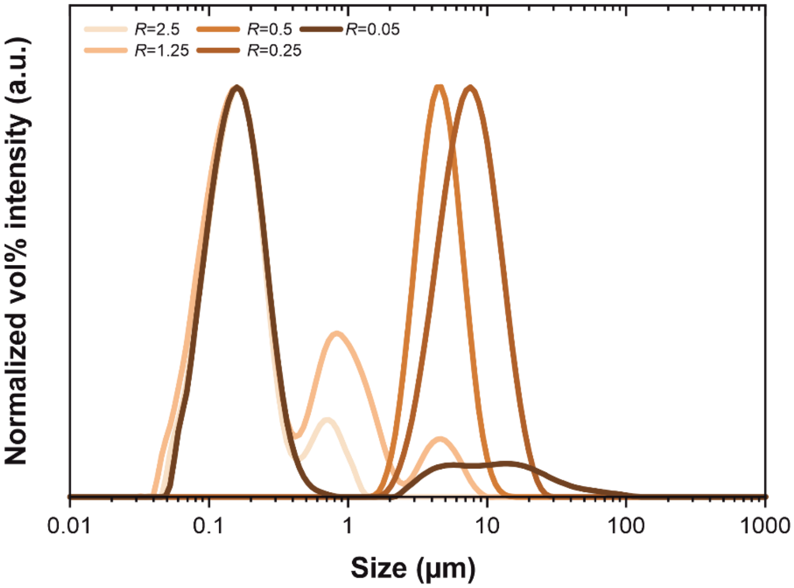

Figure S10: Laser light diffraction measurements of formed agglomerates of citric acid-capped SPIONs and amine-capped PSNPL for different *R*-values at pH~3.2. The size distribution graphs of *R*=2.5 and *R*=1.25 (highest SPION concentrations) show a distinct peak in the nano-size region around 200 nm suggesting that residual SPIONs are left in dispersion and not fully incorporated into agglomerates. Furthermore, micron-sized agglomerates between 1 µm to 10 µm can be measured, as well. These peaks represent the fraction that forms large networks of agglomerates. For lower *R*-values distinct peaks between 1 µm and 30 µm are found. Interestingly, for *R*=0.05 (lowest SPION concentration) the size distribution is governed by a peak around 100 nm to 200 nm while showing a signal between 2 µm and 100 µm at the same time. This might represent the two fractions available in the samples. One that is not incorporated into a large agglomerates and one of the formed agglomerate networks.

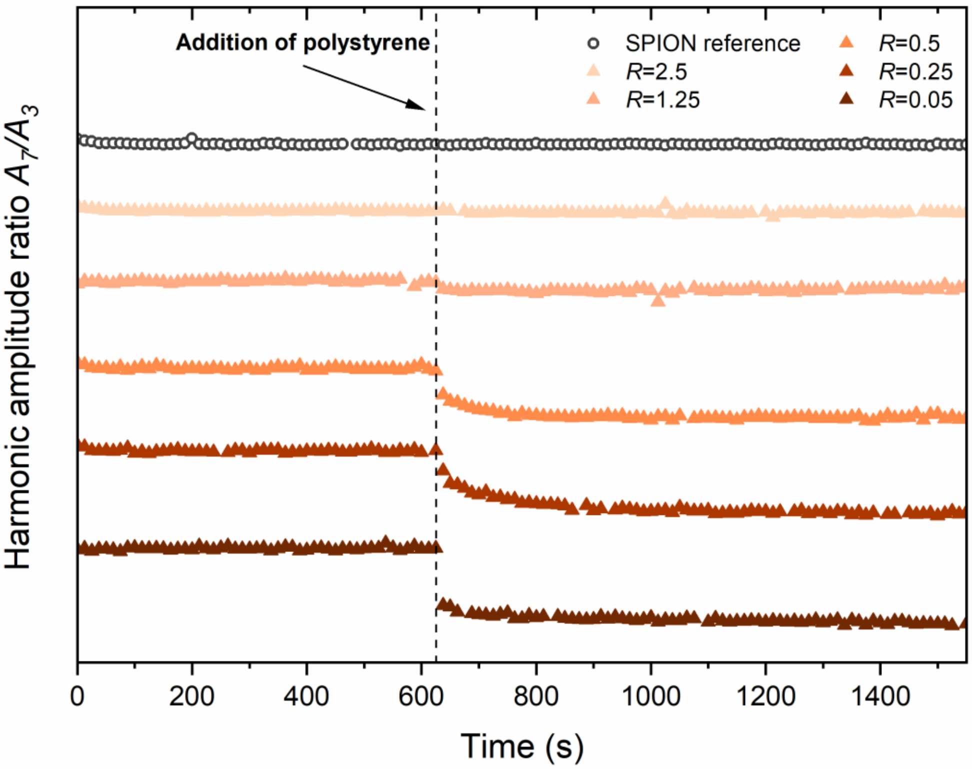

Fig. S11: *In-situ* MPS curves measured at different *R*-values at pH~3.2. The signal decay after PSNPL addition decreases with increasing particle ratio *R*. At *R*=2.5 no signal decay is observed, indicating that either single, separated SPIONs are attached to the PSNPL surface or single SPIONs are left in dispersion dominating the MPS signal.

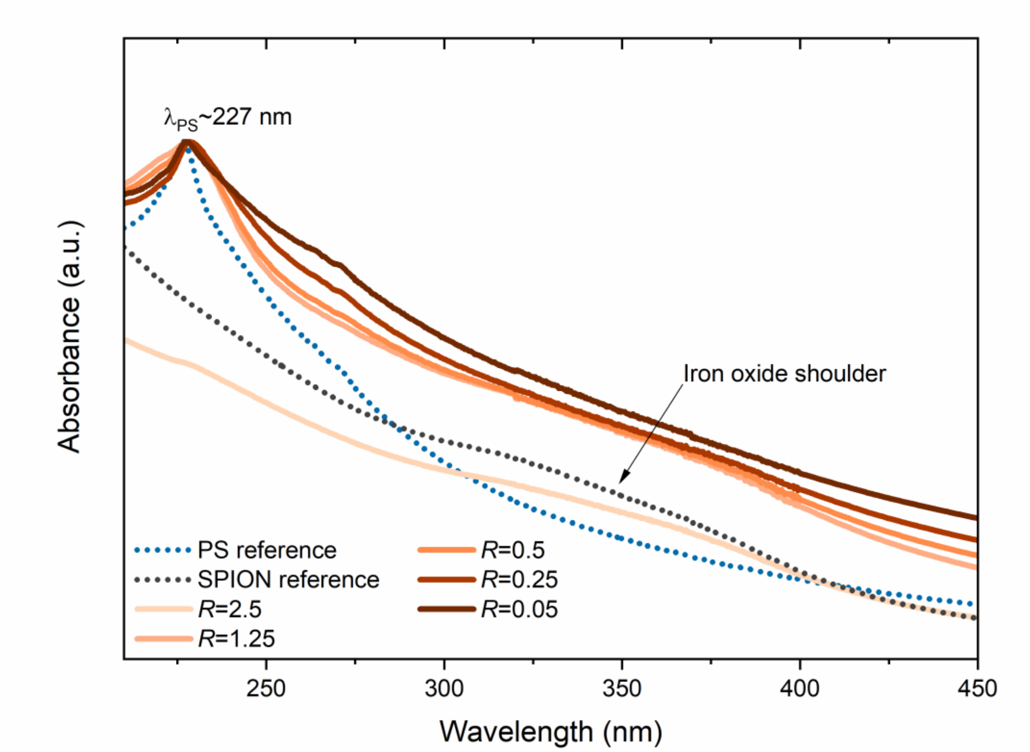

Fig. S12: UV/Vis spectra of a SPION (grey dotted line) and a PSNPL (blue dotted line) reference in comparison with suspension samples at different *R*-values after agglomerates were removed magnetically (pH~3.2). A distinct band at approximately 227 nm is observed for all *R*-values except 2.5, indicating residual polystyrene nanoparticles. In comparison to the reference spectra, an increase in absorbance between 275 nm and 400 nm can be measured, which might indicate residual SPIONs in suspension. At *R*=2.5 the absorbance is dominated by the iron oxide overall absorption, showing that iron oxide/SPIONs are the main material left in the treated water. This supports the findings of *in-situ* MPS measurements for different *R*-values.

To determine the removal efficiency of the investigated SPION systems, the nanoplastic collection capability was calculated from TGA measurements by using the following equation[7]:

$$NCC = \left(1 - \frac{x_{sample}}{x_{SPION\ reference}}\right) \cdot \left(\frac{x_{sample}}{x_{SPION\ reference}}\right)^{-1} \tag{S1}$$

with x_{sample} as the remaining mass of the investigated sample and $x_{SPION\ reference}$ as the residual mass of the corresponding SPION reference. The *NCC* values are averaged from three independent TGA measurements of SPION/PSNPL mixtures.

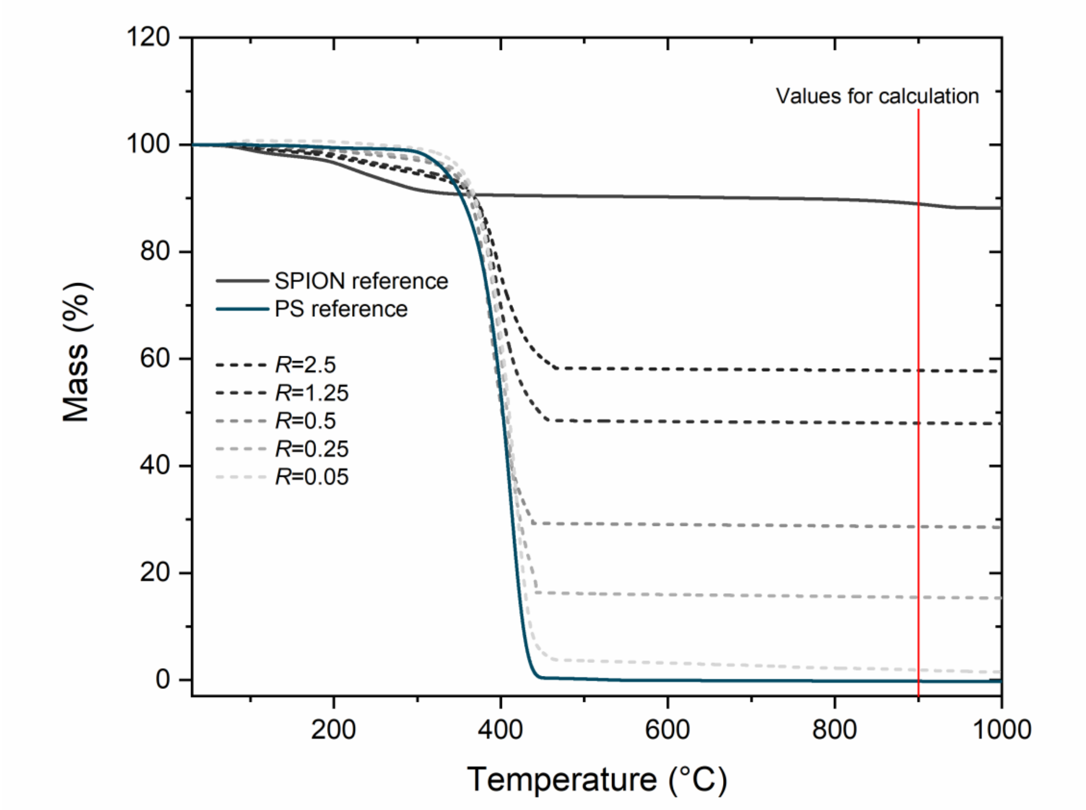

Fig. S13: Thermogravimetric analysis of CA-capped SPIONs (grey solid line), AIBA-initiated PSNPL particles (blue solid line), and magnetically collected agglomerates at different *R*-values (dashed lines). The red line indicates the values at *T*=900 °C, that were used to calculate the *NCC*.

Table S1: Calculated and theoretically achievable NCC for different *R*-values of CA-capped SPIONs and AIBA-initiated PSNPL particles.

***R*-value**	**NCC_{calc} [g g^{-1}]**	**NCC_{theo} [g g^{-1}]**	**c_{SPIONs} [mg ml^{-1}]**	**c_{PSNPL} [mg ml^{-1}]**
0.05	38.95±7.52	20	0.05	1
0.25	4.53±0.21	4	0.25	1
0.5	2.1±0.02	2	0.5	1
1.25	0.84±0.02	0.8	1.25	1
2.5	0.54±0.11	0.4	2.5	1

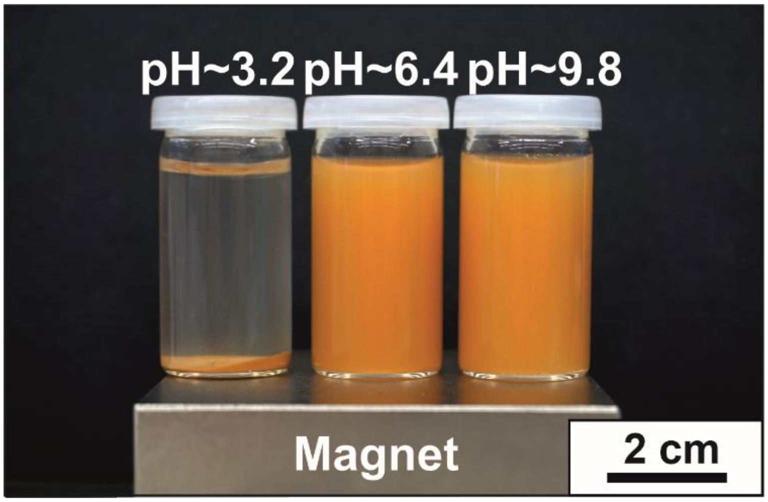

Fig. S14: Image of CA-capped SPION/AIBA-initiated PSNPL mixtures at pH~3.2, pH~6.4, and pH~9.8 (left to right). At a lower colloidal stability (pH~3.2) collectable agglomerate networks are formed. The strong EDL around the SPION/PSNPL agglomerates may prevent the formation of large agglomerate networks at pH~6.4 and 9.8. This hinders the collection of nanoparticles by an external magnetic field.

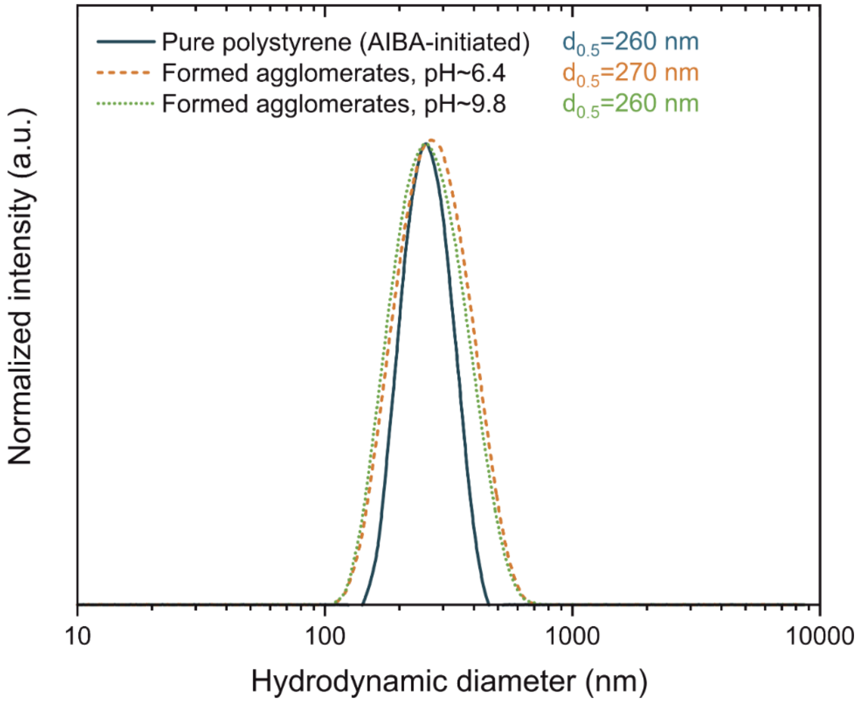

Fig. S15: Comparison of the hydrodynamic diameters of pure AIBA-initiated PSNPL particles with formed agglomerates of CA-capped SPIONs/PSNPL at pH~6.4 (orange dashed lines) and pH~9.8 (green dotted line). A slightly broader size distribution is obtained for the agglomerates, which might indicate the clustering of a few, single PSNPL decorated with SPIONs.

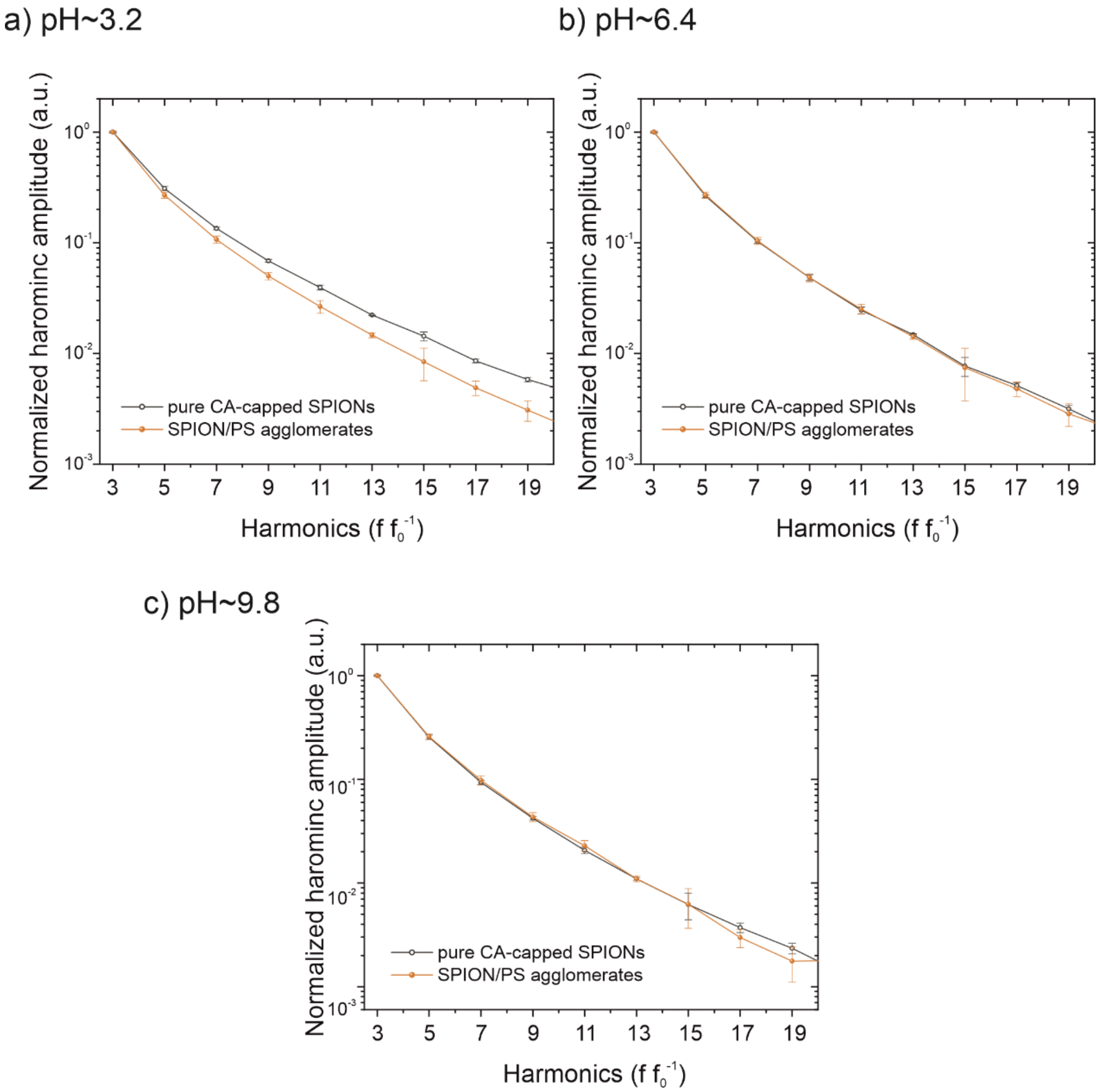

Fig. S16: MPS signal curves of a SPION reference (grey line and data points) and formed agglomerates (orange line and data points) at pH~3.2 (a), pH~6.4 (b), and pH~9.8. No significant difference in signal decay is observed at higher pH values, indicating that no agglomerate network formation takes place.

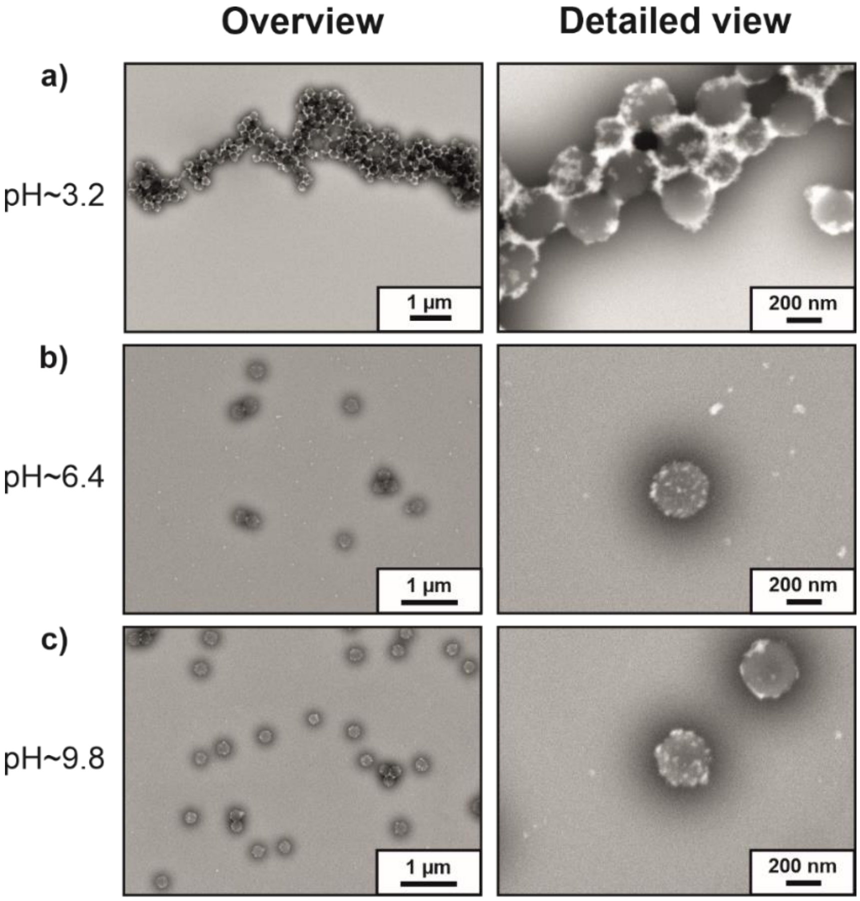

Fig. S17: Overview (left array) and detail (right array) BSE-SEM micrographs of formed agglomerates between positively charged PSNPL and negatively charged SPIONs at pH~3.2 (a), pH~6.4 (b), and pH~9.8 (c). At acidic conditions above the IEP of CA-capped SPIONs (pH>3), the electrostatic repulsion between SPIONs allows the formation of large, destabilized agglomerates, whereas at neutral and alkaline conditions the increased colloidal stability, due to higher electrostatic repulsion, prevents the formation of these large agglomerate networks as SPIONs repel each other. Instead, only single PSNPL particles are decorated with SPIONs eventually forming clusters consisting of a few PSNPL particles, which stands in accordance with DLS measurements.

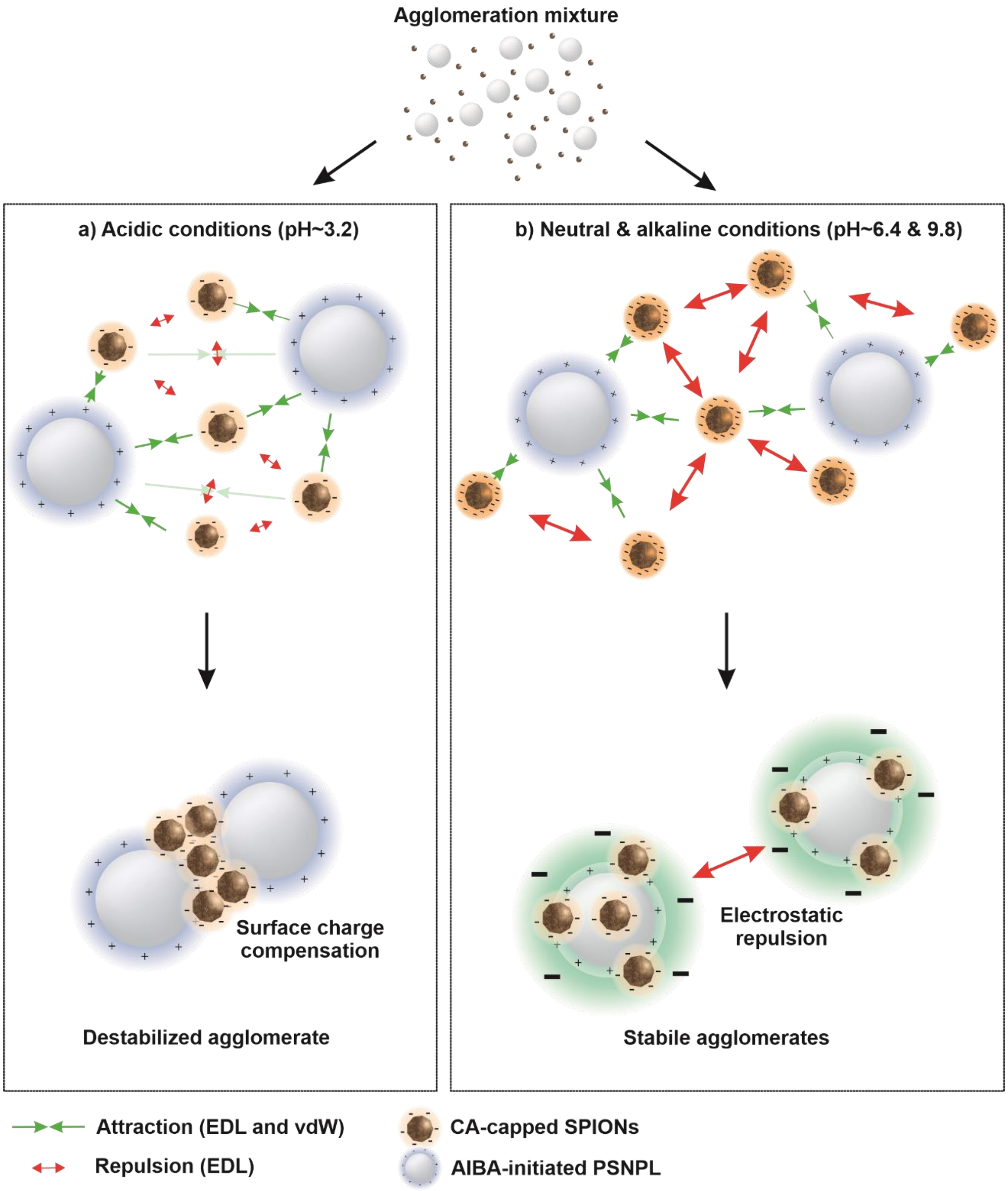

Fig. S18: Schematic illustration of the agglomeration process taking place between SPIONs and PSNPLs with oppositely charged surfaces when mixed in water with different pH values. At acidic conditions (here: pH~3.2) the surface charge compensation outweighs the repulsion between single SPIONs leading to agglomerate network formation with the observed neck-like structure (a). At neutral and alkaline conditions (here: pH~6.4 and 9.8) the repulsive forces between single SPIONs increases due to continuous deprotonation of the citric acids surface groups. The attractive forces between oppositely charged SPIONs and PSNPLs enables agglomerate formation. However, network formation seems to be prevented as the EDL of SPIONs governs the electrostatic forces in dispersion. Instead, clusters of single PSNPLs decorated with single SPIONs eventually form.

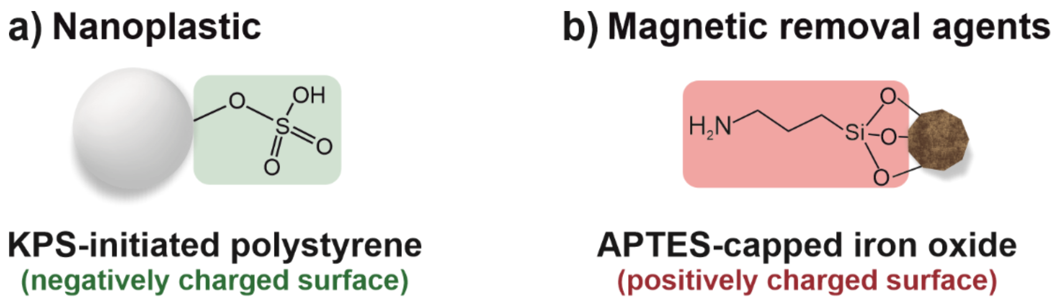

Fig. S19: Scheme of a second nanoparticle model system. Polystyrene nanoparticles were synthesized by using KPS as a polymerization initiator. By this, sulfate groups are introduced on the particle surface leading to a negative surface charge (a). (3-aminopropyl) triethoxysilane-capped SPIONs were synthesized as oppositely charged magnetic removal agents (b).

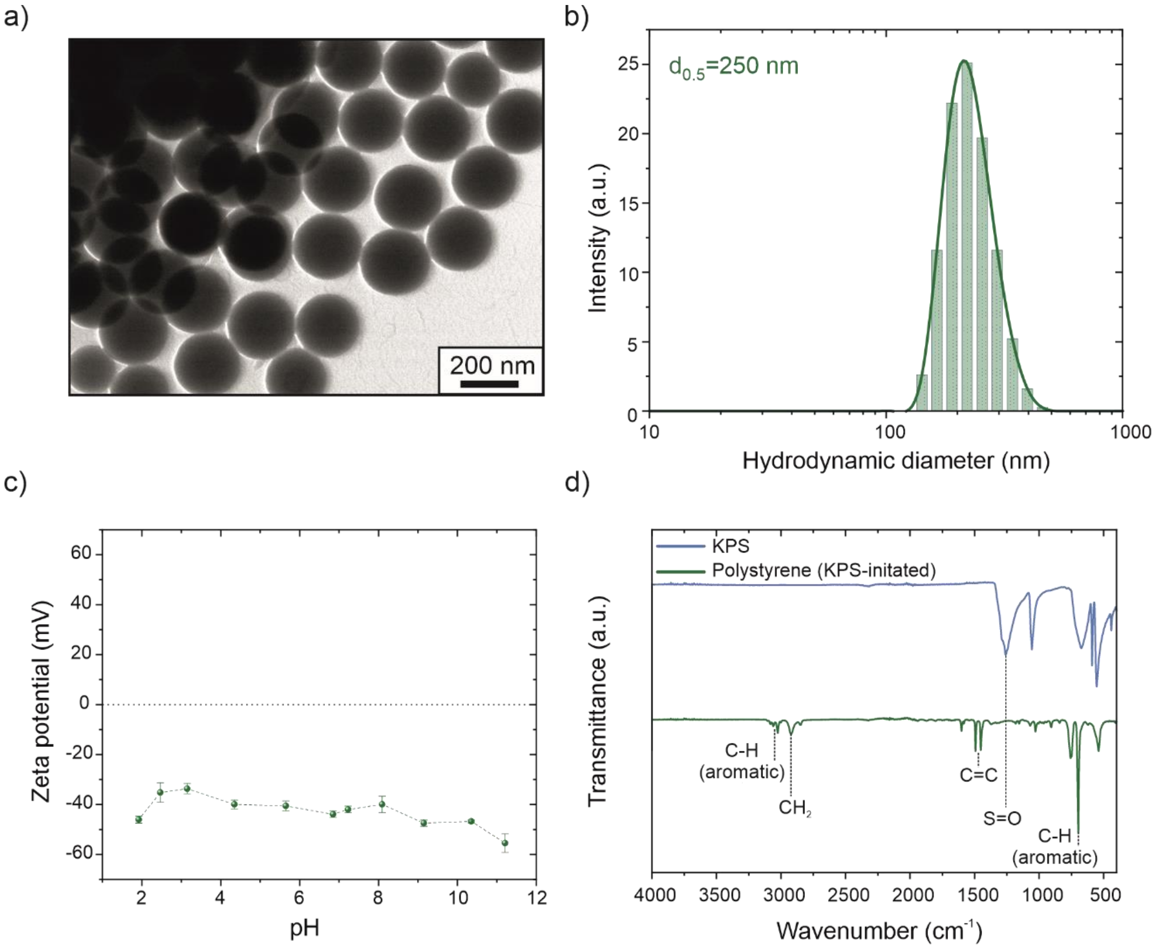

Fig. S20: Characterization of KPS-initiated polystyrene nanoparticles, synthesized by emulsion polymerization. The nanoparticle size was determined by STEM analysis (a) to be 220±17 nm and the hydrodynamic diameter was found to be $d_{0.5}$=250 nm by DLS measurements (b). Zeta potential measurements (c) showed a negative surface potential over the investigated pH range. FTIR analysis (d) indicated the typical aromatic signals of polystyrene (aromatic system: aromatic C-H stretching ~3000-3100 cm^{-1}, C=C stretching ~1400-1600 cm^{-1} and C-H bending ~700 cm^{-1}; aliphatic system: CH_2 vibrations ~2850-2950 cm^{-1}). No signal of the KPS-based surface groups could be detected (sulfate: S=O stretching ~1250-1450 cm^{-1}). However, the surface potential supports the presents of negatively charged sulfate groups.

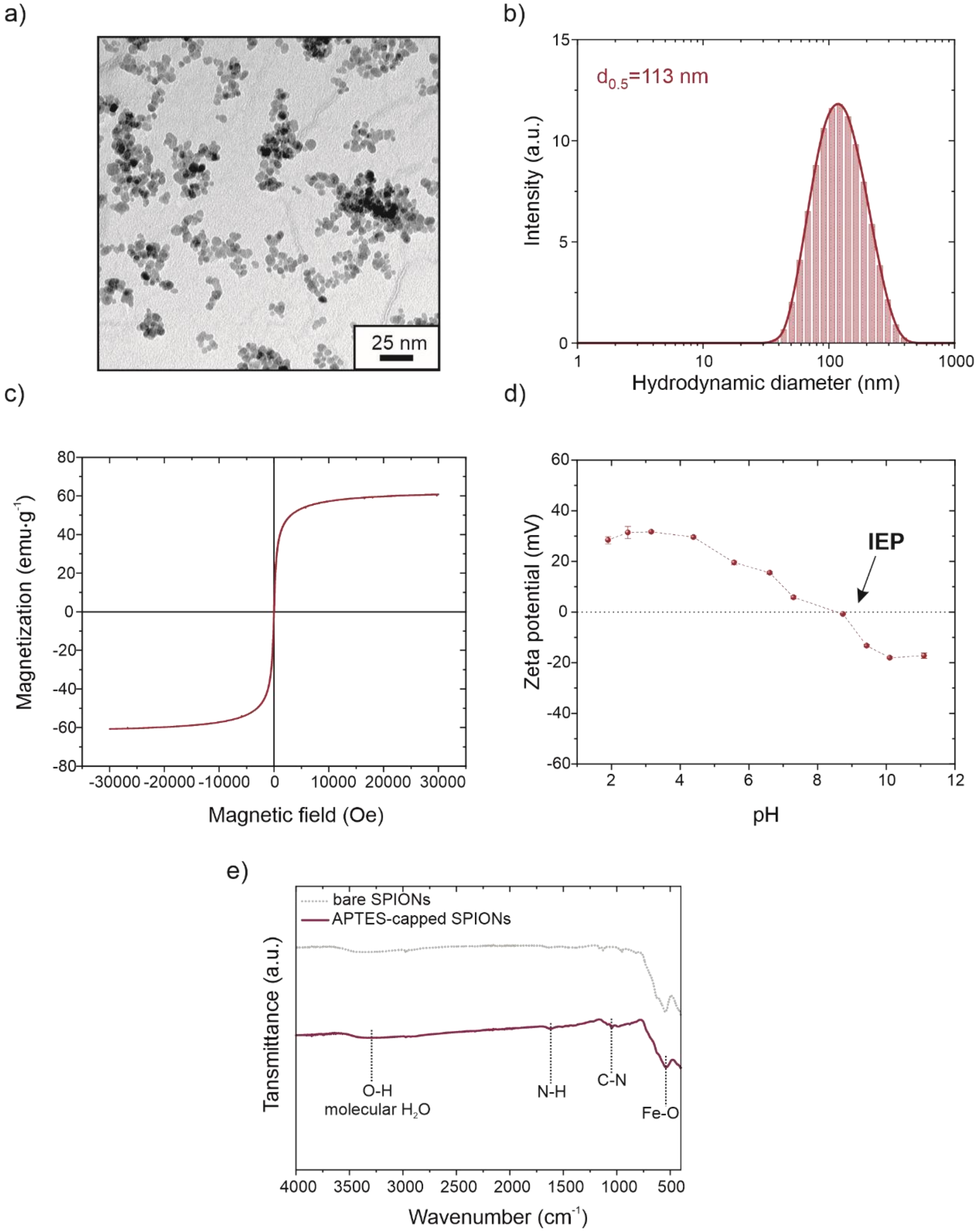

Fig. S21: Characterization of APTES-capped SPIONs. The nanoparticle size was determined by TEM analysis (a) to be 13±3 nm and the hydrodynamic diameter was found to be $d_{0.5}$=113 nm by DLS measurements (b). Comparison of TEM and DLS data suggests a tendency of APTES-capped SPIONs to agglomerate. SQUID measurements (c) revealed the superparamagnetic behavior of the synthesized nanoparticles with a saturation magnetization of 61 emu g^{-1}. Zeta potential measurements (d) showed a positive surface potential between pH~2 and pH~9, shifting into the negative region above. FTIR analysis (e) suggested the capping of SPIONs with APTES (molecular H_2O: O-H stretching ~3000-3500 cm^{-1}; primary amine: N-H bending~1630 cm^{-1}; alkyl amine: C-N stretching~1045 cm^{-1}; iron oxide: Fe-O vibrations ~550 cm^{-1}).

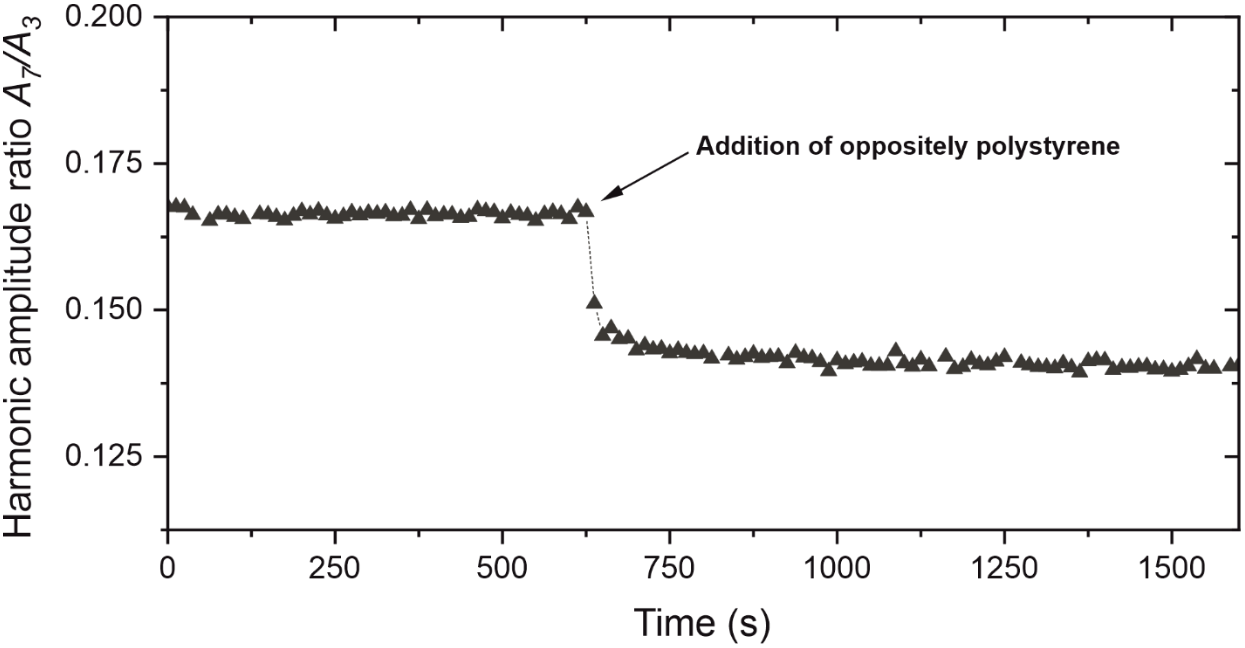

Fig. S22: Time-dependent *in-situ* MPS curve of APTES-capped SPIONs with addition of KPS-initiated PSNPL particles (R=0.5, c_{PS}=2 mg ml^{-1} and c_{SPIONs}=1 mg ml^{-1}, pH~3.2). The signal decay after PSNPL addition indicates the agglomeration between SPIONs and PSNPL particles in a large agglomerate network.

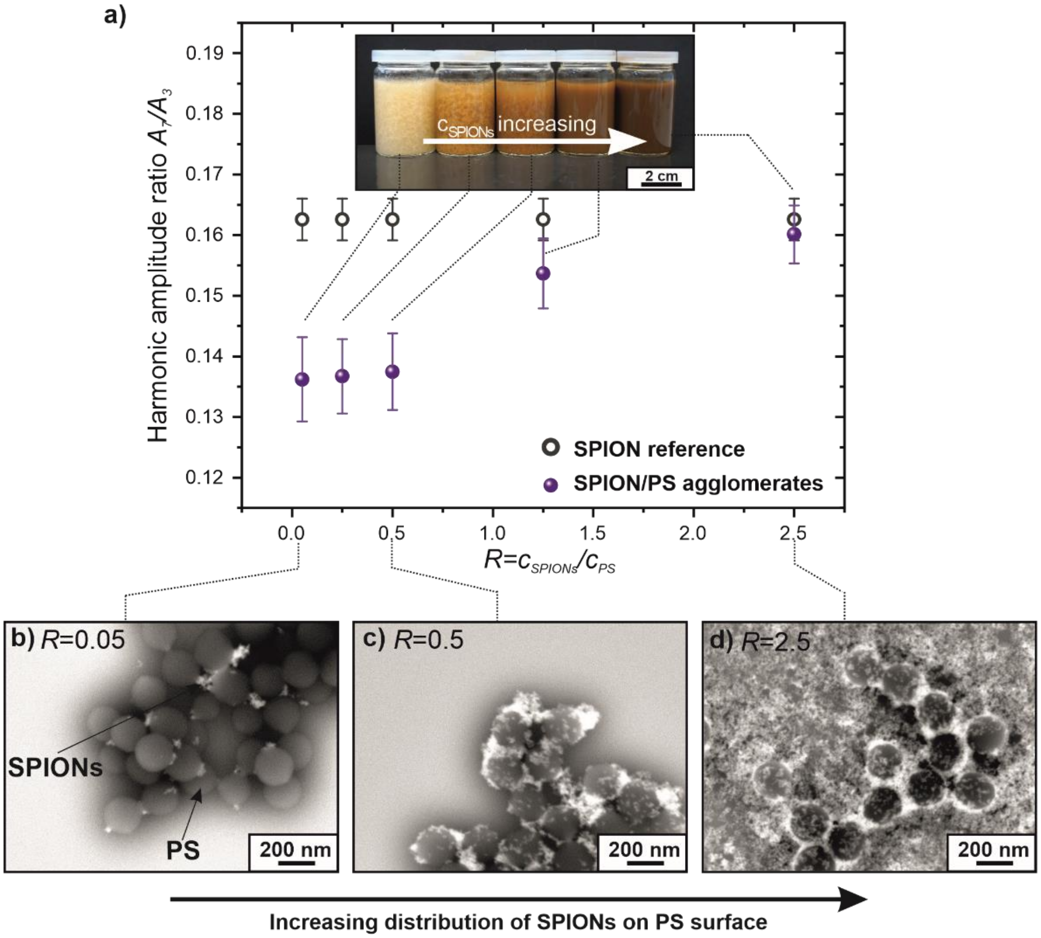

Fig. S23: Magnetic particle spectroscopy of different particle ratios *R* of APTES-capped SPIONs to KPS-initiated PSNPL at pH~3.2 (a). The harmonic amplitude ratio of the seventh to the third harmonic increases gradually with increasing R and finally approaches the signal of a pure APTES-capped SPION reference. BSE-SEM micrographs of formed agglomerates at a particle ratio *R* of 0.05 (c_{PS}=2 mg ml^{-1} and c_{SPIONs}=0.1 mg ml^{-1}) (b), 0.5 (c_{PS}=2 mg ml^{-1} and c_{SPIONs}=1 mg ml^{-1}) (c), and 2.5 (c_{PS}=2 mg ml^{-1} and c_{SPIONs}=5 mg ml^{-1}) (d). For all ratios, the formation of SPION (bright spots) necks around the PSNPL (dark spots) can be observed. With increasing SPION concentration (increasing *R*-value), the distribution of magnetic particles across the polystyrene nanoparticles enhances. The progressive separation of single SPIONs on the polystyrene surface with increasing SPION concentration could lead to the change in MPS signal. By measuring the magnetic signal of SPIONs in close proximity and isolated ones, the signal of the isolated ones would govern the signal decay leading to a harmonic amplitude comparable to the SPION reference.

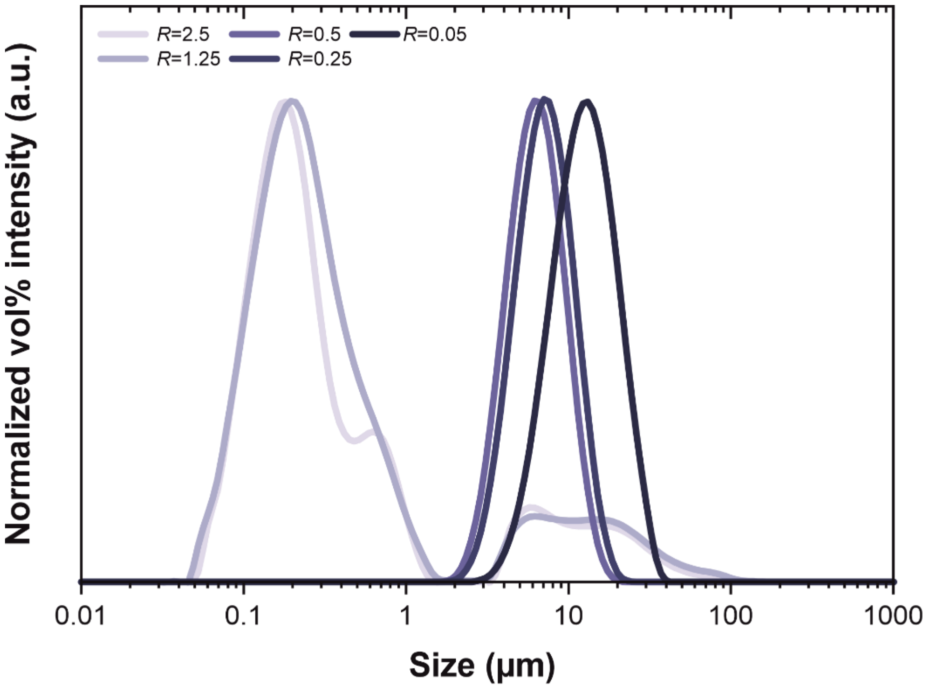

Figure S24: Laser light diffraction measurements of formed agglomerates of amine/imine-capped SPIONs and sulfate-capped PSNPL for different *R*-values at pH~3.2. The size distribution graphs of *R*=2.5 and *R*=1.25 (highest SPION concentrations) show a distinct peak in the nano-size region around 200 nm suggesting that residual SPIONs are left in dispersion and not fully incorporated into agglomerates. Furthermore, micron-sized agglomerates between 3 µm to 100 µm can be measured, as well. These peaks represent the fraction that forms large networks of agglomerates. For lower *R*-values distinct peaks between 2 µm and 20 µm are found.

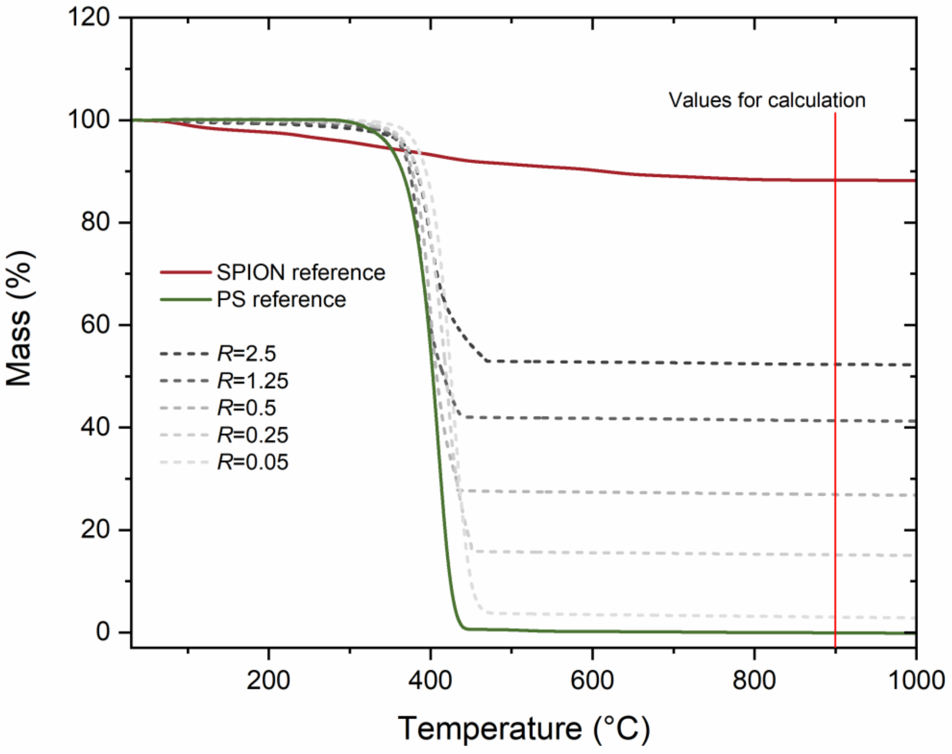

Fig. S25: Thermogravimetric analysis of APTES-capped SPIONs (dark red solid line), KPS-initiated PSNPL particles (green solid line), and magnetically collected agglomerates at different *R*-values (dashed lines). The vertical red line indicates the values at T=900 °C, that were used to calculate the *NCC*.

Table S2: Calculated and theoretically achievable values of *NCC* for different *R*-values of amine-capped SPIONs to KPS-initiated PSNPL.

***R*-value**	**NCC_{calc} [g g^{-1}]**	**NCC_{theo} [g g^{-1}]**	**c_{SPIONs} [mg ml^{-1}]**	**c_{PSNPL} [mg ml^{-1}]**
0.05	27.59±0.95	20	0.05	1
0.25	4.9±0.18	4	0.25	1
0.5	2.3±0.03	2	0.5	1
1.25	1.19±0.08	0.8	1.25	1
2.5	0.69±0.01	0.4	2.5	1

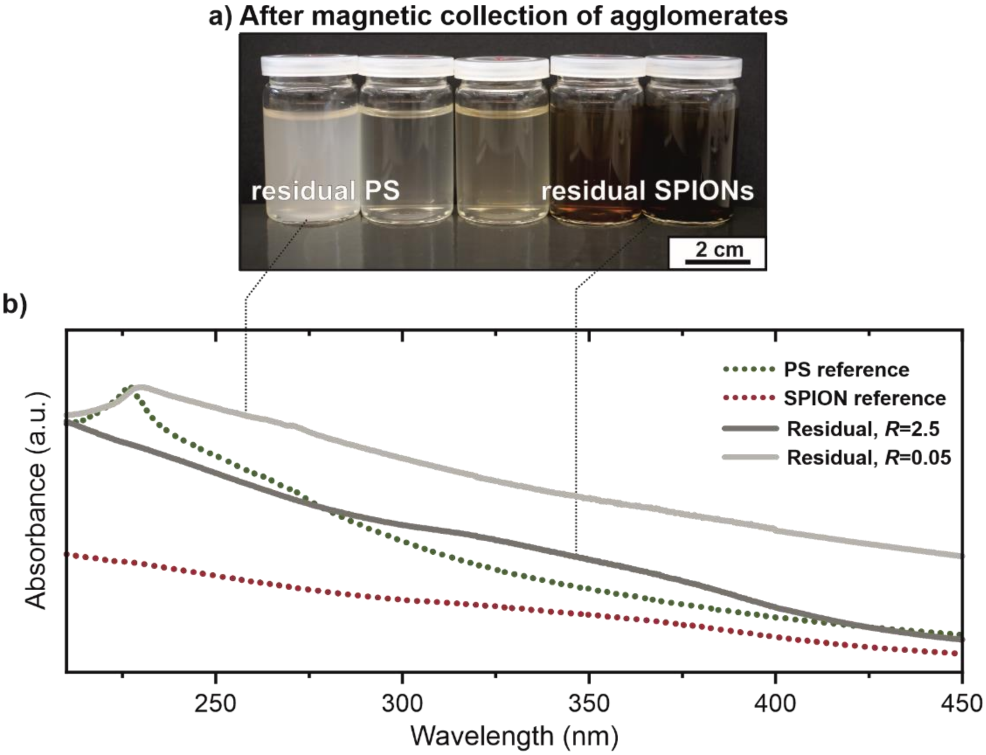

Fig. S26: Image of SPION-treated PSNPL samples with an initial PSNPL concertation of 1 mg/ml after magnetic collection of the formed agglomerates (a). Particle ratio *R* from left to right: 0.05, 0.25, 0.5, 1.25, 2.5. Low SPION concentrations leave behind polystyrene nanoplastics in the treated water, whereas high SPION concentrations lead to leftovers of SPIONs. A transparent supernatant can be observed for an *R*-value of 0.25 and 0.5, indicating a suitable particle ratio for sufficient pollutant removal. Qualitative UV/Vis spectra of the supernatants (light grey line: *R*=0.05, dark grey line: *R*=2.5) support these observations (b). The corresponding spectra display the same absorbance behavior as a dispersion of the bare reference materials (dotted lines).

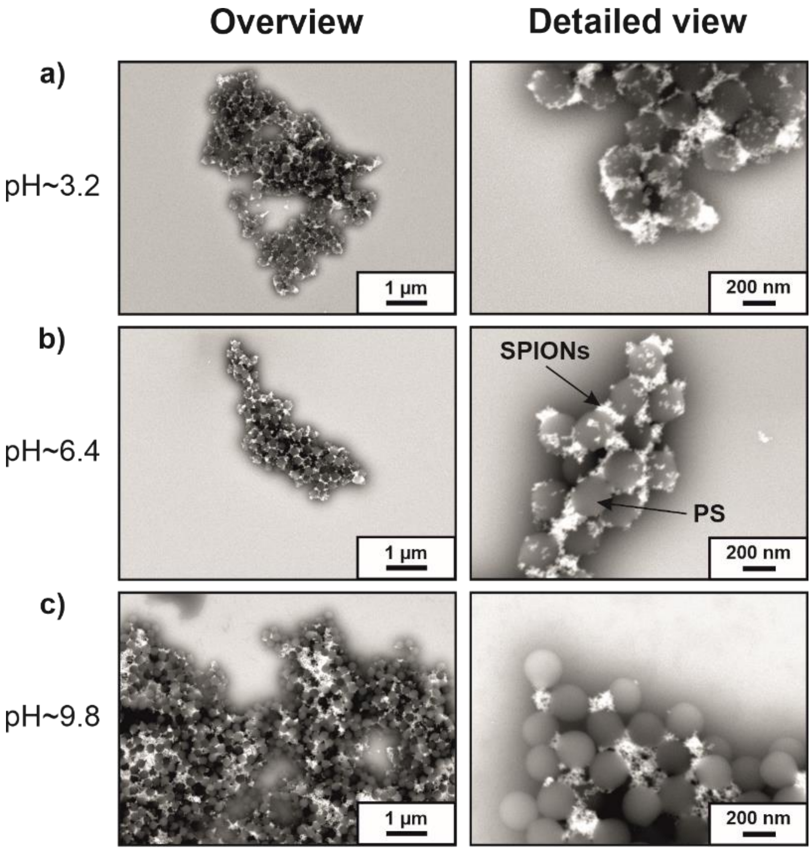

Fig. S27: Overview (left array) and detail (right array) BSE-SEM micrographs of formed agglomerates between negatively charged PSNPL and APTES-capped SPIONs at pH~3.2 (a), pH~6.4 (b), and pH~9.8 (c) (R=0.5, c_{PS}=2 mg ml^{-1} and c_{SPIONs}=1 mg ml^{-1}). At all pH values, the agglomerate formation can be observed. Interestingly, at pH~9.8 mainly large clusters of SPIONs are observed between PSNPL particles, and barely single SPIONs are met at the PSNPL surface.

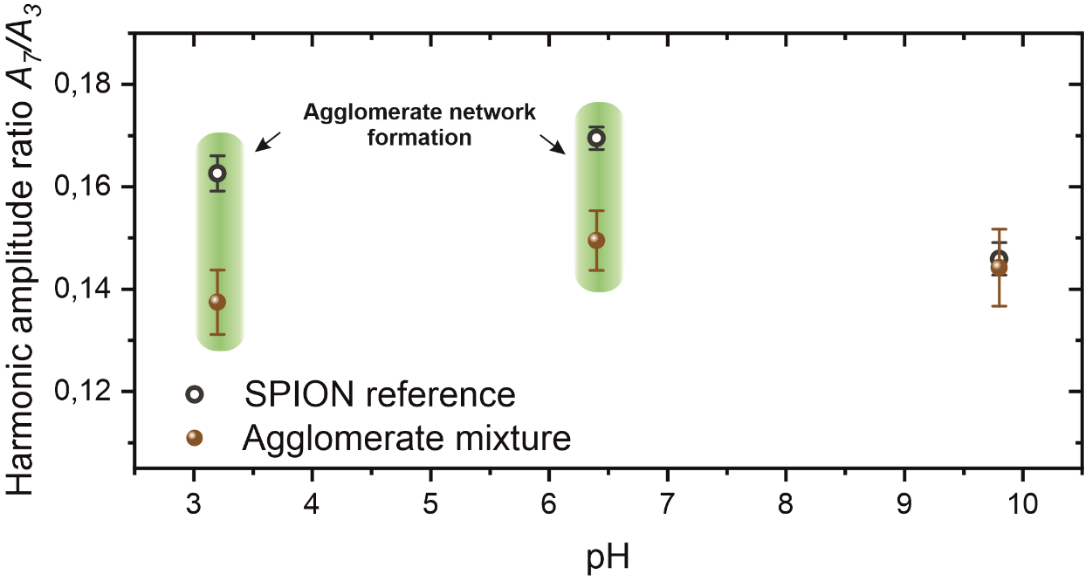

Fig. S28: Magnetic particle spectroscopy of APTES-capped SPIONs (grey data points) and APTES-capped SPION/KPS-initiated PSNPL mixtures with a particle ratio *R* of 0.5 (c_{PS}=2 mg ml^{-1} and c_{SPIONs}=1 mg ml^{-1}) in different pH regions (a). A decrease in harmonic amplitude ratio A_7/A_3 was observed only at pH~3.2 and pH~6.4 when compared to the SPION reference. This indicates the formation of an agglomerate network via MPS (green background). At pH~9.8, no significant change in A_7/A_3 was detected, although agglomerates were formed and could be magnetically collected. This indicated a pre-agglomeration of APTES-capped SPIONs due to low electrostatic repulsion at this pH value.

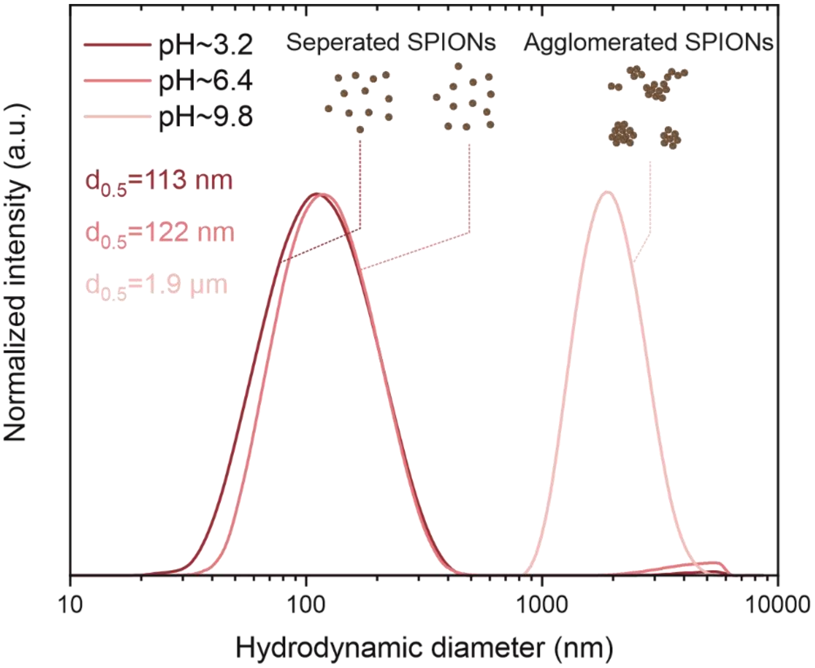

Fig. S29: Distribution of hydrodynamic diameters of APTES-capped SPIONs at different pH values. The obtained data suggest a pre-agglomeration of APTES-capped SPIONs at a pH region around 9.8, due to the close proximity to the IEP.

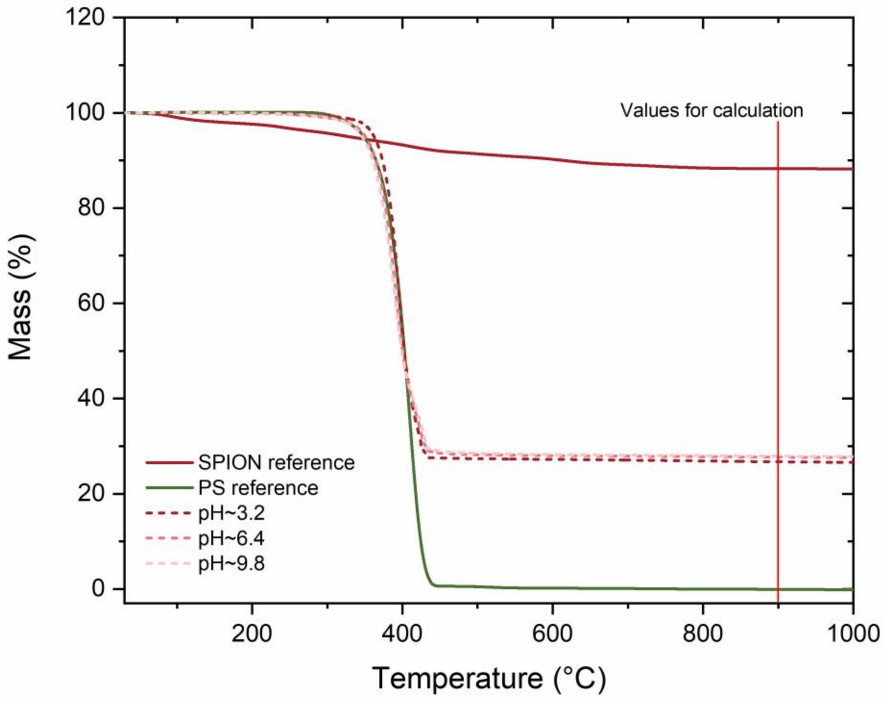

Fig. S30: Thermogravimetric analysis of agglomerates of APTES-capped SPIONs and KPS-initiated PSNPL particles collected magnetically at different pH values. The vertical red line indicates the values at *T*=900 °C, that were used to calculate the *NCC*.

Table S3: Calculated and theoretically achievable nanoplastic collection capability for different pH values of APTES-capped SPIONs.

pH	***NCC*calc** **[g g^{-1}]**	***NCC*theo** **[g g^{-1}]**	***c*SPIONs** **[mg ml^{-1}]**	***c*PSNPL** **[mg ml^{-1}]**
3.2	2.3±0.03	2	0.5	1
6.4	2.19±0.07	2	0.5	1
9.8	2.16±0.02	2	0.5	1

References

1 S. Müssig, F. Fidler, D. Haddad, K.-H. Hiller, S. Wintzheimer and K. Mandel, Supraparticles with a Magnetic Fingerprint Readable by Magnetic Particle Spectroscopy: An Alternative beyond Optical Tracers, *Adv. Mater. Technol.*, 2019, **4**, 1900300.

2 K. Wu, D. Su, R. Saha, J. Liu and J.-P. Wang, Investigating the effect of magnetic dipole–dipole interaction on magnetic particle spectroscopy: implications for magnetic nanoparticle-based bioassays and magnetic particle imaging, *J. Phys. D: Appl. Phys.*, 2019, **52**, 335002.

3 S. Biederer, T. Knopp, T. F. Sattel, K. Lüdtke-Buzug, B. Gleich, J. Weizenecker, J. Borgert and T. M. Buzug, Magnetization response spectroscopy of superparamagnetic nanoparticles for magnetic particle imaging, *J. Phys. D: Appl. Phys.*, 2009, **42**, 205007.

4 F. Fidler, M. Steinke, A. Kraupner, C. Gruttner, K.-H. Hiller, A. Briel, F. Westphal, H. Walles and P. M. Jakob, Stem Cell Vitality Assessment Using Magnetic Particle Spectroscopy, *IEEE transactions on magnetics*, 2015, **51**, 1–4.

5 C. Kuhlmann, A. P. Khandhar, R. M. Ferguson, S. Kemp, T. Wawrzik, M. Schilling, K. M. Krishnan and F. Ludwig, Drive-field Frequency Dependent MPI Performance of Single-Core Magnetite Nanoparticle Tracers, *IEEE transactions on magnetics*, 2015, **51**.

6 K. Wu, D. Su, R. Saha, J. Liu, V. K. Chugh and J.-P. Wang, Magnetic Particle Spectroscopy: A Short Review of Applications Using Magnetic Nanoparticles, *ACS Appl. Nano Mater.*, 2020, **3**, 4972–4989.

7 M. Sarcletti, H. Park, J. Wirth, S. Englisch, A. Eigen, D. Drobek, D. Vivod, B. Friedrich, R. Tietze, C. Alexiou, D. Zahn, B. Apeleo Zubiri, E. Spiecker and M. Halik, The remediation of nano-/microplastics from water, *Materials Today*, 2021, **48**, 38–46.